

Dirac Nodal Lines and Nodal Loops in a Topological Kagome Superconductor CsV_3Sb_5

Zhanyang Hao^{1,2,*}, Yongqing Cai^{1,2,*}, Yixuan Liu^{1,2,*}, Yuan Wang^{1,2,*}, Xuelei Sui³, Xiao-Ming Ma^{1,2}, Zecheng Shen^{1,2}, Zhicheng Jiang⁴, Yichen Yang⁴, Wanling Liu⁴, Qi Jiang⁴, Zhengtai Liu⁴, Mao Ye⁴, Dawei Shen⁴, Yi Liu⁵, Shengtao Cui⁵, Jiabin Chen³, Le Wang^{1,2}, Cai Liu^{1,2}, Junhao Lin¹, Jianfeng Wang^{6,3,#}, Bing Huang³, Jia-Wei Mei^{1,2,7,#} and Chaoyu Chen^{1,2,#}

¹ Shenzhen Institute for Quantum Science and Engineering, and Department of Physics, Southern University of Science and Technology, Shenzhen 518055, China

² International Quantum Academy, and Shenzhen Branch, Hefei National Laboratory, Futian District, Shenzhen 518048, China

³ Beijing Computational Science Research Center, Beijing 100193, China

⁴ State Key Laboratory of Functional Materials for Informatics and Center for Excellence in Superconducting Electronics, Shanghai Institute of Microsystem and Information Technology, Chinese Academy of Sciences, Shanghai 200050, China

⁵ National Synchrotron Radiation Laboratory, University of Science and Technology of China, Hefei 230029, China

⁶ School of Physics, Beihang University, Beijing 100191, China

⁷ Shenzhen Key Laboratory of Advanced Quantum Functional Materials and Devices, Southern University of Science and Technology, Shenzhen 518055, China

* These authors contributed equally to this work.

#Correspondence should be addressed to J.W. (wangjf06@buaa.edu.cn), J.M. (meijw@sustech.edu.cn) and C.C. (chency@sustech.edu.cn)

Abstract

The intertwining of charge order, superconductivity and band topology has promoted the $AV_3\text{Sb}_5$ ($A=\text{K, Rb, Cs}$) family of materials to the center of attention in condensed matter physics. Underlying those mysterious macroscopic properties such as giant anomalous Hall conductivity (AHC) and chiral charge density wave is their nontrivial band topology. While there have been numerous experimental and theoretical works investigating the nontrivial band structure and especially the van Hove singularities, the exact topological phase of this family remains to be clarified. In this work, we identify CsV_3Sb_5 as a Dirac nodal line semimetal based on the observation of multiple Dirac nodal lines and loops close to the Fermi level. Combining photoemission spectroscopy and density functional theory, we identify two groups of Dirac nodal lines along k_z direction and one group of Dirac nodal loops in the $A-H-L$ plane. These nodal loops are located at the Fermi level within the instrumental resolution limit. Importantly, our first-principle analyses indicate that these nodal loops may be a crucial source of the mysterious giant AHC observed. Our results not only provide a clear picture to categorize the band structure topology of this family of materials, but also suggest the dominant role of topological nodal loops in shaping their transport behavior.

Introduction:

At the heart of the current condensed matter physics lies the interplay between band topology and certain symmetry breaking orders [1], as such interplay could give rise to novel quantum phases and phenomena such as quantum anomalous Hall effect in Chern insulator [2-5], Majorana mode in topological superconductor [6-10], axion dynamics in axion insulator [11,12] and so on. In this context, the recently discovered AV_3Sb_5 ($A=K, Rb, Cs$) family of materials [13] have attracted tremendous research interests due to their coexisting nontrivial band topology arising from kagome lattice geometry, unconventional superconductivity, and charge density wave (CDW). These materials share the same layered structure with two-dimensional (2D) transition metal V kagome lattice [13-15], resulting in multiple Dirac cones and the rich nature of van Hove singularities in their electronic structure as demonstrated via angle-resolved photoemission spectroscopy (ARPES) [16-29] measurements and density-functional theory (DFT) calculations [30]. Superconductivity was discovered with $T_c = 0.93 K$ for KV_3Sb_5 [14], $T_c = 0.92 K$ for RbV_3Sb_5 [15], and $T_c = 2.5 K$ for CsV_3Sb_5 [16], respectively. Meanwhile, at $T^* \sim 80 - 100 K$ a CDW order was observed [13-16,18,31,32], whose relationship with superconductivity is still under debate [20,31,33-38]. Nevertheless, recent experimental and theoretical works have suggested the unconventional nature of both orders [18,31,37-41].

Surprisingly, giant anomalous Hall conductivity (AHC) up to the order of $10^4 \Omega^{-1}cm^{-1}$ was observed in nonmagnetic KV_3Sb_5 [42] and CsV_3Sb_5 [39]. Recent muon spin spectroscopy [43] measurement demonstrates the absence of local V^{4+} moments. So the AHC has no magnetic origin, but may be associated with the chiral CDW order [31,39,42,44]. In this sense, it is of key importance to correctly understand their topological band structure for the electronic origin of the giant AHC. It was first proposed that this family of materials can be categorized as \mathbb{Z}_2 topological metals with a continuous direct gap [16]. Subsequent ARPES measurements have revealed multiple Dirac crossings and the rich nature of van Hove singularities (VHSs) close to the Fermi level (E_F) [16-28]. Nevertheless, under the combined \mathcal{PT} symmetry with inversion symmetry \mathcal{P} and time reversal symmetry \mathcal{T} , this system should contain Dirac nodal lines rather than isolated Dirac points [30] in its three-dimensional (3D) Brillouin zone (BZ). This suggests that the exact topological phase of AV_3Sb_5 ($A=K, Rb, Cs$) family remains to be clarified and the necessity of a full 3D BZ band investigation to identify its topological band features.

In this work, we present a comprehensive ARPES spectral mapping covering the full 3D BZ of topological kagome superconductor CsV_3Sb_5 . Combining ARPES and DFT calculation, we identify two types of Dirac nodal lines in a shallow energy region ($\leq 0.3 eV$) below E_F . The first type consists of two groups of nodal lines along k_z direction, arising from the quasi-2D nature of the kagome lattice. The second type consists of one group of nodal loops surrounding the H points in $k_x - k_y$ plane, *i.e.*, $A - H - L$ plane. The Dirac energies of these nodal loops are almost equal to E_F within the instrumental resolution limit. The satisfactory agreement between ARPES and DFT fully corroborates the existence of these low-energy Dirac nodal lines and loops. Importantly, our first-principle analyses indicate that these nodal loops may provide dominant source of Berry curvature and thus the giant AHC. Our results not only represent a clear clarification of the topological band structure in the kagome AV_3Sb_5 ($A=K, Rb, Cs$) family of materials, but also suggest nodal loops as the electronic source of the exotic transport response of the host materials.

Results:

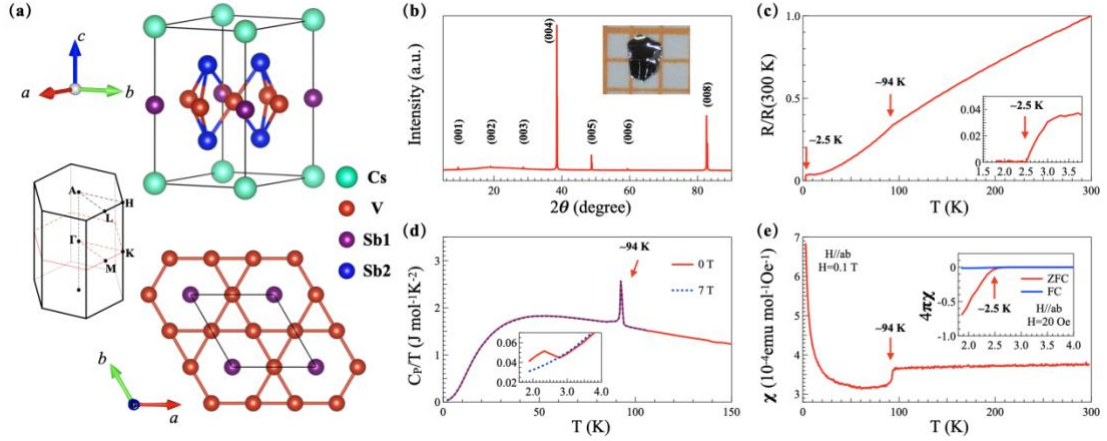


Fig. 1. Crystal structure and characterization of single-crystalline CsV_3Sb_5 . (a) Crystal structure of CsV_3Sb_5 . The V atoms construct a kagome lattice, the Sb1 atoms are in the center of the V hexagon and the Sb2 atoms form a honeycomb lattice above and below the kagome layer. The left inset shows the corresponding 3D BZ and the high-symmetry points. (b) Single-crystal XRD pattern of the (00*l*) plane. The inset shows the optical image of the CsV_3Sb_5 crystal placed on the 1 mm grid paper. (c), (d) and (e) Temperature-dependent resistivity ratio, heat capacity, and magnetic susceptibility measurements of CsV_3Sb_5 single crystal. Phase transitions indicating the charge density wave can be observed at around 94 K. All the three insets exhibit the bulk superconductivity transition around 2.5 K.

Single crystals of CsV_3Sb_5 adopt a kagome structure of V atoms with a space group of $P6/mmm$ [13], as shown in Fig. 1(a). The Sb1 atoms are in the center of the V hexagons and the Sb2 atoms compose the antimony layers which are sandwiched by the V kagome layers and Cs layers. The X-ray diffraction (XRD) pattern of (00*l*) plane is exhibited in Fig. 1(b), which indicates the high crystalline quality. The lattice parameter of the *c*-axis obtained from XRD data is about 9.308 Å, which is also consistent with the previous study [13]. For ARPES measurement, the cleavage plane is parallel to the *ab* plane (inset of Fig. 1(b)) and perpendicular to the *c* axis direction.

In Fig. 1(c), an obvious kink at ~ 94 K can be seen from the curve which is related to the CDW phase transition, and an apparent bulk superconducting transition feature exists at ~ 2.5 K (inset of Fig. 1(c)). Similarly, detailed temperature-dependent heat capacity and magnetization measurements were performed systematically. From Fig. 1(d), one can see that a sharp CDW transition peak at ~ 94 K exists for both 0 T and 7 T magnetic field. In contrast, the superconductivity transition occurs at ~ 2.5 K under the 0 T magnetic field and is suppressed under 7 T magnetic field. For the magnetic susceptibility data in Fig. 1(e), under a 0.1 T magnetic field, there is an obvious drop at ~ 94 K. The low temperature magnetic susceptibility with field-cooling (FC) and zero-field-cooling (ZFC) measurements at 20 Oe clearly shows the onset of superconductivity at ~ 2.5 K (inset of Fig. 1(e)). Note that the magnetic field is parallel to the *ab* plane in magnetization measurement and along the *c*-axis in heat capacity measurement. For ARPES measurement through this work, the sample temperature was kept at 10 K unless specified.

It is noted that while the structural signature of CDW has been clearly observed [31,32,36,40,41,45-47], the corresponding electronic signature, *e.g.*, folded band, is absent in most of the ARPES measurements [16-27]. In this work, we shall treat the ARPES spectra in and out of the CDW phase equally.

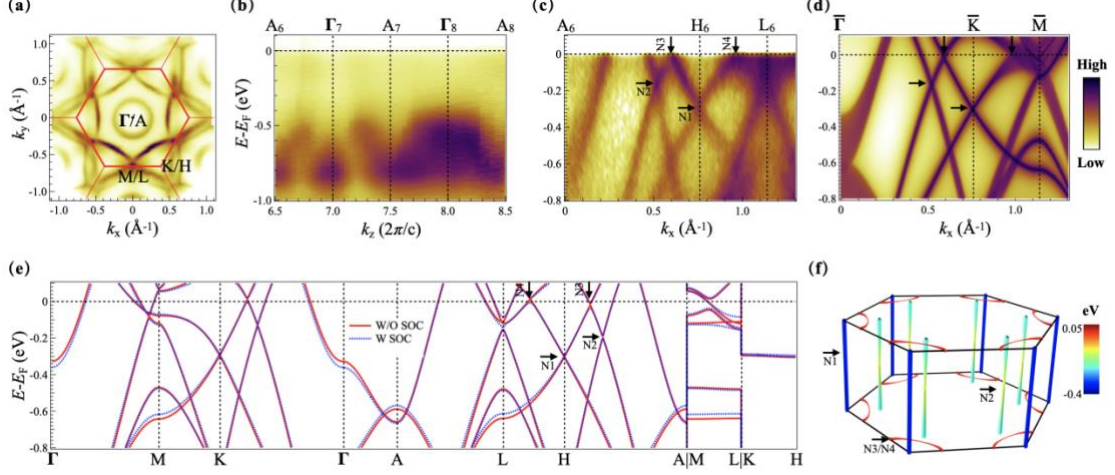


Fig. 2. General electronic structure with multiple Dirac nodal lines and loops in CsV_3Sb_5 revealed by ARPES observations and DFT calculations. (a) Fermi surface mapping in 2D BZ, where the red lines plot the BZ boundaries with high-symmetry points indicated. (b) Photon energy-dependent spectra for photoemission intensity from the BZ center Γ/A points. (c) Spectra taken along momentum cuts $A_6 - H_6 - L_6$. Black arrows indicate the existence of 4 Dirac nodes labeled as “N1” to “N4”. (d) Spectra along the $\bar{\Gamma} - \bar{K} - \bar{M}$ path from the projection of DFT calculated bands onto surface BZ. (e) DFT calculated electronic structure along all high-symmetry paths. Red solid lines represent bands without spin-orbit coupling (SOC) while blue dashed lines are results with SOC included. (f) Visualization of Dirac nodal lines and loops formed by nodes N1, N2, N3 and N4 in the 3D BZ from DFT calculations. The different colors represent their energy relative to E_F . Note that the calculated E_F is slightly shifted upward in order to match the experimental results.

The layered nature of the kagome lattice in CsV_3Sb_5 makes its band dispersion along k_z direction quite weak. While the DFT calculations predict a $\sim 350 \text{ meV}$ dispersion along $\Gamma - A$ direction [16,30,48], such k_z dependence cannot be found from recently reported ARPES results [16-27]. It is thus of importance to examine this discrepancy. Judging from the Fermi surface geometry, we align the ARPES momentum cut to $\bar{\Gamma} - \bar{K} - \bar{M}$ high-symmetry path ($k_y = 0$ path in Fig. 2(a)) and perform photon energy dependent measurement for a photon energy range of 70 – 130 eV. As shown in Fig. 2(b), the spectral intensity from $\bar{\Gamma}$ point exhibits a clear periodic dispersion, which corresponds to the $\Gamma - A$ dispersion as predicted by DFT calculations in Fig. 2(e) [16,30,48]. This periodicity helps us to identify the bulk Γ and A points of the 3D BZ as specified in Fig. 2(b). In this way, the k_z location of all the following ARPES spectra cuts and $k_x - k_y$ mappings can be approximately determined.

ARPES spectra along the high-symmetry cut $A_6 - H_6 - L_6$ is shown in Fig. 2(c). Projection of DFT calculated dispersion onto the surface BZ path $\bar{\Gamma} - \bar{K} - \bar{M}$ is also presented in Fig. 2(d) for comparison. Both ARPES and DFT results show consistent features as discussed below. One parabolic electron pocket can be found around Γ/A , whose band bottom contributes to the k_z

dispersion observed in Fig. 2(b). Besides that, all the bands are linearly dispersed in a narrow energy region below E_F . These bands cross each other and form Dirac nodes. We have identified as many as four Dirac nodes with Dirac energy $E_D \leq 0.3 \text{ eV}$, as indicated by black arrows in Figs. 2(c, d). Sorted according to binding energy, these nodes are labeled as “N1” up to “N4”. Dirac node N1 represents the Dirac cone at K/H point with $E_D \approx 0.3 \text{ eV}$ while N2 the Dirac cone between Γ/A and K/H points with $E_D \approx 0.15 \text{ eV}$. When moving to E_F , two nodes, N3 and N4, appear. Node N3 comes from the crossing between the upper Dirac cones of N1 and N2, and N4 shares a similar origin. The exact energy position of N3 and N4 may be slightly below or up E_F , yet we consider them effectively located at E_F since their Dirac energy is comparable to or even smaller than our practical energy resolution limit and the energy distribution width of ARPES measured bands.

The emergence of multiple Dirac nodes as discussed above has been captured in recent ARPES results [16-27] but their k_z dependence in 3D BZ lacks systematic discussion. In Fig. 2(e), we present the DFT calculated electronic structure along all the high-symmetry paths in the 3D BZ of CsV_3Sb_5 . From the calculations, for a narrow energy range close to E_F , while the bands along $\Gamma - A$ and $M - L$ possess a clear k_z dispersion, the bands along $K - H$ are almost k_z independent. This brings about two important electronic features. On the one hand, the Dirac nodes N1 and N2 look almost the same at paths $\Gamma - K - M$ and $A - H - L$, suggesting the formation of Dirac nodal lines along k_z direction in the 3D BZ. On the other hand, the nodes N3 and N4 are located not only at almost the same energy, but also at the same upper Dirac cone of node N1, suggesting the possibility of one closed nodal loop at the Fermi level surrounding H point. In Fig. 2(f), the DFT predicted distributions of these four Dirac nodes are shown in the 3D BZ. It is clearly demonstrated that there exist two groups of straight nodal lines along the k_z direction and one group of closed nodal loops surrounding H point at the $A - H - L$ plane.

From a point of view of symmetry, these three groups of nodal lines/loops are protected by different symmetries. The CsV_3Sb_5 crystal has a point group of D_{6h} , including inversion I , C_6 rotation, six vertical mirrors σ_v and one horizontal mirror σ_h symmetries. The nodal lines formed by N1 (blue in Fig. 2(f)) are fixed along $K - H$, which are protected by the C_{3v} subgroup along this high-symmetry line; while the nodal lines formed by N2 (nearly green in Fig. 2(f)) are in the three $\Gamma - K - H - A$ planes and protected by the σ_v mirror planes. The nodal loops formed by N3/N4 surrounding H point at $A - H - L$ plane (red in Fig. 2(f)) are protected by the σ_h mirror symmetry. Any local perturbations preserving the related symmetries will not break these nodal lines/loops. It is noted that the SOC effect is weak, and it only opens a small gap for the Dirac nodes and nodal lines/loops (see Fig. 2(e)), consistent with the previous DFT works [16,30,48]. In the following, we will use ARPES data to visualize these nodal lines and nodal loops separately.

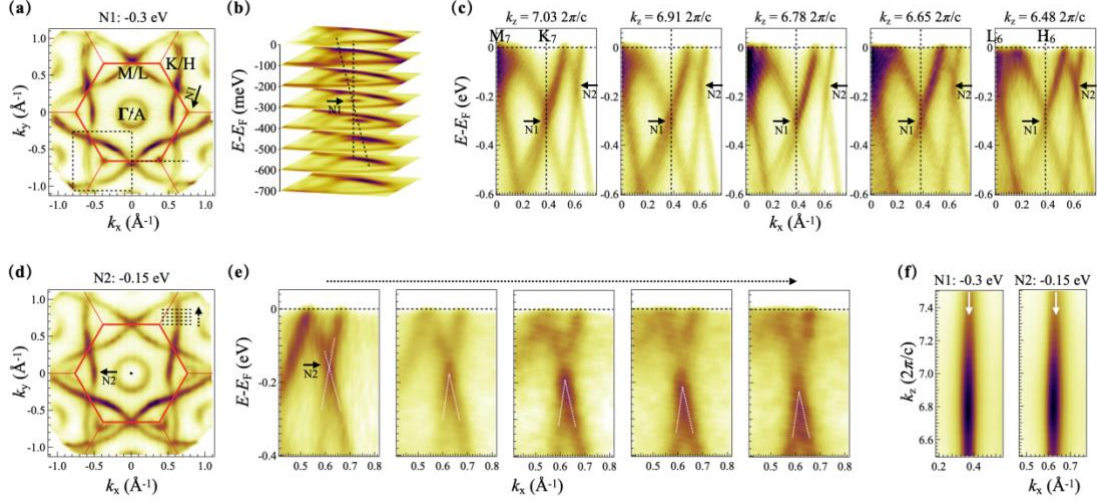


Fig. 3. Visualizations of Dirac nodal lines along k_z direction formed by nodes N1 and N2. (a) Constant energy contours (CECs) in $k_x - k_y$ plane at a binding energy of ~ 0.3 eV, which shows the Dirac nodal point (black arrow) formed by node N1. (b) CECs in $k_x - k_y$ plane at a series of binding energies. Black dashed lines indicate the N1 Dirac cone dispersion. (c) Spectra taken along a high-symmetric $M/L - K/H - \Gamma/A$ direction at a series of k_z planes with black arrows highlighting the positions of N1 and N2. (d) CEC in $k_x - k_y$ plane at a binding energy of ~ 0.15 eV, which shows the Dirac nodal point (black arrow) formed by node N2. (e) Spectra from a series of momentum cuts whose positions are indicated by black dashed lines in (d). White dashed lines highlight the gap opening of the Dirac cone when moving away from node N2. (f) Direct visualizations of N1, N2 Dirac nodal lines in the $k_z - k_x$ plane from the CECs at the corresponding binding energies.

Concerning the nodal lines along k_z direction, we start with node N1. Fig. 3(a) presents the constant energy contours (CECs) at its binding energy of ~ 0.3 eV, which shows a nodal point at K/H point as indicated by the black arrow. By analyzing its shape evolution in CECs at a series of binding energies (Fig. 3(b)), we find that the node N1 forms a triangularly deformed Dirac cone in $k_x - k_y$ plane. The evolution of this Dirac cone along k_z direction is presented in Fig. 3(c) at five selected k_z planes. Despite some intensity variations, the dispersion of N1 Dirac cone shows no noticeable changes from K_7 to H_6 , suggesting the existence of N1 nodal line along k_z direction. In the left panel of Fig. 3(f), the CEC at its corresponding energy of ~ 0.3 eV in $k_x - k_z$ plane directly visualizes this N1 nodal line.

For node N2, its CEC in $k_x - k_y$ plane shows a deformed, closed hexagon in the first 2D BZ (Fig. 3(d)), suggesting a nodal loop formation in $k_x - k_y$ plane. However, by examining its detailed dispersion along different momentum cuts as shown in Fig. 3(e), we find that the gapless N2 Dirac cone only exists along the high-symmetric $\bar{\Gamma} - \bar{K}$ path. When moving away from this high-symmetry path, this Dirac cone gradually opens a gap. This suggests that the node N2, like N1, also forms nodal points in $k_x - k_z$ plane. The k_z evolution of N2 shown together with N1 in Fig. 3(c) draws the same conclusion that the nodal lines are formed along k_z direction. In the right panel of Fig. 3(f), the CEC at its corresponding energy of ~ 0.15 eV in $k_x - k_z$ plane directly visualizes this N2 nodal line.

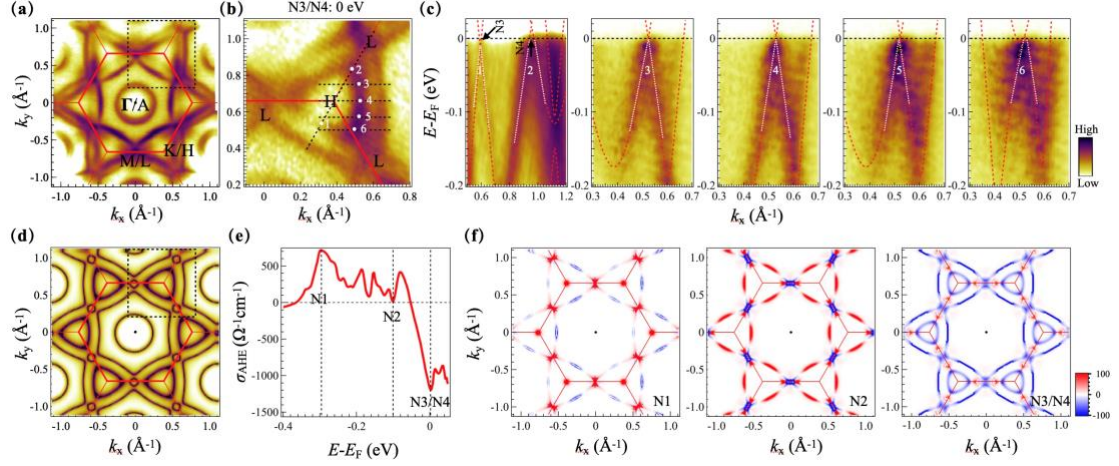


Fig. 4. Visualizations of Dirac nodal loops at Fermi surface formed by nodes N3/N4 and calculated AHC and Berry curvatures contributed by the observed nodal lines/loops. (a) CEC in $k_x - k_y$ plane at E_F . (b) CEC in the momentum region indicated by black dashed box in (a). White dots labeled by numbers indicate the nodes determined from spectra analysis in (c). (c) Spectra taken from a series of momentum cuts whose positions are indicated by black dashed lines in (b). White dotted lines with labeled numbers indicate the dispersion evolution and momentum evolution of node N3/N4. DFT calculated dispersion evolution along the same momentum cuts are demonstrated by the red dashed lines. (d) Simulated Fermi surface by DFT calculations. (e) Calculated AHC as a function of binding energy. (f) Calculated Berry curvature distributions in $A - H - L$ plane at different binding energies of $-0.3 eV$, $-0.1 eV$ and $0 eV$, respectively.

Concerning Dirac nodes N3 and N4, we first analyze their CEC at the Fermi level in the $A - H - L$ plane. Note that from the DFT calculated dispersion (Fig. 2(e)), the node N4 doesn't exist in the $\Gamma - K - M$ plane. Fig. 4(b) highlights the Fermi surface in the momentum region surrounding the H point in the CEC, as indicated by black dashed box in Fig. 4(a). In this CEC, one can see two closed triangles surrounding the H point. While the outer triangle comes from the upper Dirac band of node N2, the inner one is formed by the Dirac node N3/N4. To fully demonstrate this, we extract several spectra from a series of momentum cuts as denoted by the black dashed lines in Fig. 4(b). As shown in Fig. 4(c), the linear dispersions are observed and highlighted by the white dotted lines in these spectra. All show the signatures of Dirac nodes close to the Fermi level, which are labeled by numbers in white. These Dirac nodes are connected together to form a closed loop (Fig. 4(b)) considering the three-fold rotation symmetry. In Fig. 4(d), we plot the simulated Fermi surface by the DFT calculations in the $A - H - L$ plane. The satisfactory agreement between ARPES (Fig. 4(a)) and DFT (Fig. 4(d)) fully corroborates the existence of Dirac nodal loops at the Fermi surface.

Finally, we discuss the possible contributions of these Dirac nodal loops/lines to the exotic giant AHC observed by recent experiments[39,42]. Although there is no observation of magnetic order, the unconventional chiral CDW of CsV_3Sb_5 can break the time-reversal symmetry[32,43], leading to the appearance of anomalous Hall effect. A modal estimation based on the gapped Dirac nodes around M point gives rise to AHC of $10^2 \Omega^{-1}cm^{-1}$ [31], which is two orders of magnitude lower

than the observed value. Here, we emphasize that the nodal loops/lines observed here can contribute more additional Berry curvatures and greater AHC once the time-reversal symmetry is broken, similar to $\text{Co}_3\text{Sn}_2\text{S}_2$ [49]. To demonstrate this point, a ferromagnetic state of CsV_3Sb_5 is employed to simulate the situation of time-reversal symmetry breaking, which can be achieved by DFT+ U calculations with a Hubbard $U = 2 \text{ eV}$ (the average local moment on each V atom is $0.27 \mu_B$, see method section). The calculated AHC under different binding energies is shown in Fig. 4(e). Large AHC is achieved at some binding energies, especially near E_F which can reach to a giant value of $10^3 \Omega^{-1}\text{cm}^{-1}$. Here, three typical binding energies ($-0.3, -0.1$ and 0 eV) are selected to visualize the Berry curvature distributions in the BZ, as shown in Fig. 4(f). At the binding energy of -0.3 eV , the calculated AHC is $\sim 750 \Omega^{-1}\text{cm}^{-1}$, and the Berry curvatures are mainly distributed around the L (M) and H (K) points, reflecting the contributions of N1 nodal lines. At the binding energy of -0.1 eV , the AHC is calculated nearly zero, arising from the cancellation of the Berry curvatures from the positive contributions of N2 nodal lines and negative contributions around the L (M) point. At the Fermi level, the calculated AHC is as high as $\sim -1250 \Omega^{-1}\text{cm}^{-1}$, and the nodal loops formed by N3/N4 play a dominant role in the Berry curvature distributions. Therefore, these Dirac nodal loops contribute to the large Berry curvature, which is directly responsible for the giant AHC observed in AV_3Sb_5 family of materials.

Discussion:

While numerous ARPES and DFT works have focused on the detailed band structure of AV_3Sb_5 family of materials, particularly the VHSs at the \bar{M} point as they are closely related to the unconventional CDW order, it is still necessary to have a clear picture concerning their global electronic structure and the exact topological phase. By examining the electronic structure of CsV_3Sb_5 in its full 3D BZ from both experimental and theoretical aspects, we could identify it as a Dirac nodal line semimetal, especially with one group of nodal loops at the Fermi surface. Our results not only provide a clear picture to categorize the band structure topology of this family of materials, but also suggest the potential role of Dirac nodal loops in shaping their transport behavior. Concerning the giant AHC observed in this family [39,42], the lack of local or global magnetic moments suggests the intrinsic nature of AHC and the key role of electronic structure [13,43]. Under the chiral CDW order, besides the Dirac nodes around the M point which gives rise to AHC of two orders of magnitude lower than the observed value [31], our results point out that the presence of multiple nodal loops at the Fermi level around bulk H point could contribute additional larger Berry curvature and bring forth AHC whose value can reach as high as $\sim 1250 \Omega^{-1}\text{cm}^{-1}$. This offers new insight into the intrinsic origin of giant AHC in this family and calls for further theoretical and experimental investigations.

ACKNOWLEDGEMENTS

We thank Prof. Haizhou Lu, Qihang Liu, Wen Huang for helpful discussions. This work is supported by National Natural Science Foundation of China (NSFC) (Grants Nos. 12074163 and 12004030), the Shenzhen High-level Special Fund (Grants No. G02206304 and No. G02206404), the Guangdong Innovative and Entrepreneurial Research Team Program (Grants No. 2017ZT07C062 and No. 2019ZT08C044), Shenzhen Science and Technology Program (Grant No. KQTD20190929173815000), the University Innovative Team in Guangdong Province (No.

2020KCXTD001), Shenzhen Key Laboratory of Advanced Quantum Functional Materials and Devices (No. ZDSYS20190902092905285), Guangdong Basic and Applied Basic Research Foundation (No. 2020B1515120100), and China Postdoctoral Science Foundation (2020M682780).

Materials and Methods

Sample growth and characterization

CsV₃Sb₅ single crystals were synthesized by the self-flux method. High purity Cs (clump), V (powder) and Sb (ball) were mixed with a ratio of 2:1:6 in the glovebox and placed into an alumina crucible. The crucible was then double sealed into an evacuated quartz tube under high pressure to avoid oxidization during the reaction. In the furnace, the double sealed quartz tube was heated up to 500°C and kept at this temperature for 10 hours. Then the temperature was increased to 1050°C, after 12 hours the temperature was slowly decreased down to 650°C in 200 hours. After the heating procedure, the quartz tube was taken into the centrifuge to remove the excess flux. Many millimeter-sized hexagonal CsV₃Sb₅ single crystals were obtained.

The structure of the crystals was determined by x-ray diffraction with Cu K α radiation at room temperature using a Rigaku MiniFlex diffractometer. The diffraction pattern can be well indexed by the (00l) reflections.

Transport, heat capacity and magnetic measurements

Magnetization measurements were performed by Magnetic Property Measurement System (MPMS3, Quantum Design). Quartz paddle was used, and the magnetic field was perpendicular to the *c* - axis to minimize the diamagnetic contribution. Heat capacity and resistivity measurements were performed by Physical Property Measurement System (PPMS, Quantum Design). For resistivity, a standard four-probe method was employed with a probe current of 0.5mA. And the electrical current was in the *ab* plane. For heat capacity, the selected single crystal was approximately 1.5 mm width and length, and Apezion N-grease was used to ensure the connection with heat capacity stage.

ARPES measurement

ARPES measurements were performed at the BL03U beamline of the Shanghai Synchrotron Radiation Facility and the BL-13U beamline of the National Synchrotron Radiation Laboratory (NSRL) both with DA30L electron analysers. The energy and angular resolution were set at 20 meV and less than 0.05°, respectively. Samples were cleaved *in situ* under ultra-high vacuum conditions with pressure better than 5×10^{-11} mbar and temperatures below 20 K.

First-principles calculations

The first-principles calculations are performed using the Vienna ab initio simulation package [50] within the projector augmented wave method [51] and the generalized gradient approximation of the Perdew-Burke-Ernzerhof [52] exchange-correlation functional. The plane-wave basis with an energy cutoff of 400 eV and the Γ -centered $12 \times 12 \times 6$ *k*-point meshes are adopted. Employing the experimental lattice constants of $a=b=5.495$ Å and $c=9.308$ Å, the crystal structure of CsV₃Sb₅ is relaxed with van der Waals correction [53] until the residual forces on each atom is less than 0.005 eV/Å. The ferromagnetic and 120°-antiferromagnetic states with different Hubbard *U* are tested,

which gives a ferromagnetic ground state with a small spin polarization energy when $U > 0.8$ eV. The SOC effect is also considered in part of our calculations. A tight-binding (TB) Hamiltonian based on the maximally localized Wannier functions (MLWF) [54] is constructed to get the energy eigenvalues and eigenstates for further Fermi surface plot using the WannierTools package [55]. In order to simulate the time-reversal symmetry breaking to calculate the AHC of CsV₃Sb₅, a ferromagnetic ground state is employed by adopting DFT+ U calculations with $U = 2$ eV, which gives a spin polarization energy of 0.1 eV/unit cell and an average local moment of $0.27 \mu_B/V$. Then, the AHC and Berry curvatures are calculated by constructing MLWF and using WannierTools package.

- [1] Yoshinori Tokura, Masashi Kawasaki & Naoto Nagaosa. Emergent functions of quantum materials. *Nature Physics* **13**, 1056-1068, doi:10.1038/nphys4274 (2017).
- [2] N. Peter Armitage & Liang Wu. On the matter of topological insulators as magnetoelectrics. *SciPost Physics* **6**, doi:10.21468/SciPostPhys.6.4.046 (2019).
- [3] Yoshinori Tokura, Kenji Yasuda & Atsushi Tsukazaki. Magnetic topological insulators. *Nature Reviews Physics* **1**, 126-143, doi:10.1038/s42254-018-0011-5 (2019).
- [4] Cui-Zu Chang, Jinsong Zhang, Xiao Feng, Jie Shen, Zuocheng Zhang, Minghua Guo, Kang Li, Yunbo Ou, Pang Wei, Li-Li Wang, Zhong-Qing Ji, Yang Feng, Shuaihua Ji, Xi Chen, Jinfeng Jia, Xi Dai, Zhong Fang, Shou-Cheng Zhang, Ke He, Yayu Wang, Li Lu, Xu-Cun Ma & Qi-Kun Xue. Experimental Observation of the Quantum Anomalous Hall Effect in a Magnetic Topological Insulator. *Science* **340**, 167, doi:10.1126/science.1234414 (2013).
- [5] Rui Yu, Wei Zhang, Hai-Jun Zhang, Shou-Cheng Zhang, Xi Dai & Zhong Fang. Quantized Anomalous Hall Effect in Magnetic Topological Insulators. *Science* **329**, 61-64, doi:10.1126/science.1187485 (2010).
- [6] Steven R. Elliott & Marcel Franz. Colloquium: Majorana fermions in nuclear, particle, and solid-state physics. *Reviews of Modern Physics* **87**, 137-163, doi:10.1103/RevModPhys.87.137 (2015).
- [7] Chetan Nayak, Steven H. Simon, Ady Stern, Michael Freedman & Sankar Das Sarma. Non-Abelian anyons and topological quantum computation. *Reviews of Modern Physics* **80**, 1083-1159, doi:10.1103/RevModPhys.80.1083 (2008).
- [8] B. Lian, X. Q. Sun, A. Vaezi, X. L. Qi & S. C. Zhang. Topological quantum computation based on chiral Majorana fermions. *Proc Natl Acad Sci U S A* **115**, 10938-10942, doi:10.1073/pnas.1810003115 (2018).
- [9] K. Yasuda, M. Mogi, R. Yoshimi, A. Tsukazaki, K. S. Takahashi, M. Kawasaki, F. Kagawa & Y. Tokura. Quantized chiral edge conduction on domain walls of a magnetic topological insulator. *Science* **358**, 1311, doi:10.1126/science.aan5991 (2017).
- [10] Zhenyu Wang, Jorge Olivares Rodriguez, Lin Jiao, Sean Howard, Martin Graham, G. D. Gu, Taylor L. Hughes, Dirk K. Morr & Vidya Madhavan. Evidence for dispersing 1D Majorana channels in an iron-based superconductor. *Science* **367**, 104, doi:10.1126/science.aaw8419 (2020).
- [11] Liang Wu, M. Salehi, N. Koirala, J. Moon, S. Oh & N. P. Armitage. Quantized Faraday and Kerr rotation and axion electrodynamics of a 3D topological insulator. *Science* **354**, 1124-

- 1127, doi:10.1126/science.aaf5541 (2016).
- [12] Dennis M. Nenzo, Christina A. C. Garcia, Johannes Gooth, Claudia Felser & Prineha Narang. Axion physics in condensed-matter systems. *Nature Reviews Physics* **2**, 682–696, doi:10.1038/s42254-020-0240-2 (2020).
- [13] Brenden R. Ortiz, Lídia C. Gomes, Jennifer R. Morey, Michal Winiarski, Mitchell Bordelon, John S. Mangum, Iain W. H. Oswald, Jose A. Rodriguez-Rivera, James R. Neilson, Stephen D. Wilson, Elif Ertekin, Tyrel M. McQueen & Eric S. Toberer. New kagome prototype materials: discovery of KV3Sb5, RbV3Sb5, and CsV3Sb5. *Physical Review Materials* **3**, doi:10.1103/PhysRevMaterials.3.094407 (2019).
- [14] Brenden R. Ortiz, Paul M. Sarte, Eric M. Kenney, Michael J. Graf, Samuel M. L. Teicher, Ram Seshadri & Stephen D. Wilson. Superconductivity in the Z2 kagome metal KV3Sb5. *Physical Review Materials* **5**, doi:10.1103/PhysRevMaterials.5.034801 (2021).
- [15] Qiangwei Yin, Zhijun Tu, Chunsheng Gong, Yang Fu, Shaohua Yan & Hechang Lei. Superconductivity and Normal-State Properties of Kagome Metal RbV3Sb5 Single Crystals. *Chinese Physics Letters* **38**, doi:10.1088/0256-307x/38/3/037403 (2021).
- [16] B. R. Ortiz, S. M. L. Teicher, Y. Hu, J. L. Zuo, P. M. Sarte, E. C. Schueller, A. M. M. Abeykoon, M. J. Krogstad, S. Rosenkranz, R. Osborn, R. Seshadri, L. Balents, J. He & S. D. Wilson. CsV3Sb5: A Z2 Topological Kagome Metal with a Superconducting Ground State. *Phys Rev Lett* **125**, 247002, doi:10.1103/PhysRevLett.125.247002 (2020).
- [17] Hailan Luo et al. Electronic Nature of Charge Density Wave and Electron-Phonon Coupling in Kagome Superconductor KV3Sb5. *arXiv: 2107.02688* (2021).
- [18] H. X. Li et al. Observation of Unconventional Charge Density Wave without Acoustic Phonon Anomaly in Kagome Superconductors AV3Sb5 (A=Rb,Cs). *arXiv: 2103.09769* (2021).
- [19] Mingu Kang et al. Twofold van Hove singularity and origin of charge order in topological kagome superconductor CsV3Sb5. *arXiv: 2105.01689* (2021).
- [20] Rui Lou et al. Charge-Density-Wave-Induced Peak-Dip-Hump Structure and Flat Band in the Kagome Superconductor CsV3Sb5. *arXiv: 2106.06497* (2021).
- [21] Soohyun Cho et al. Emergence of new van Hove singularities in the charge density wave state of a topological kagome metal RbV3Sb5. *arXiv:2105.05117* (2021).
- [22] Yong Hu et al. Charge-order-assisted topological surface states and flat bands in the kagome superconductor CsV3Sb5. *arXiv: 2104.12725* (2021).
- [23] Yong Hu et al. Rich Nature of Van Hove Singularities in Kagome Superconductor CsV3Sb5. *arXiv: 2106.05922* (2021).
- [24] Yang Luo et al. Distinct band reconstructions in kagome superconductor CsV3Sb5. *arXiv: 2106.01248* (2021).
- [25] Zhonghao Liu et al. Temperature-induced band renormalization and Lifshitz transition in a kagome superconductor RbV3Sb5. *arXiv: 2104.01125* (2021).
- [26] Zhengguo Wang et al. Distinctive momentum dependent charge-density-wave gap observed in CsV3Sb5 superconductor with topological Kagome lattice. *arXiv: 2104.05556* (2021).
- [27] Kosuke Nakayama et al. Multiple Energy Scales and Anisotropic Energy Gap in the Charge-Density-Wave Phase of Kagome Superconductor CsV3Sb5. *ArXiv: 2104.08042* (2021).

- [28] Yongqing Cai et al. Emergence of Quantum Confinement in Topological Kagome Superconductor CsV3Sb5 family. *arXiv:2109.12778* (2021).
- [29] Yixuan Liu et al. Doping evolution of superconductivity, charge order and band topology in hole-doped topological kagome superconductors Cs(V1-xTix)3Sb5. *arXiv:2110.12651* (2021).
- [30] Jianzhou Zhao et al. Electronic correlations in the normal state of kagome superconductor KV3Sb5. *arXiv: 2103.15078* (2021).
- [31] Y. X. Jiang, J. X. Yin, M. M. Denner, N. Shumiya, B. R. Ortiz, G. Xu, Z. Guguchia, J. He, M. S. Hossain, X. Liu, J. Ruff, L. Kautzsch, S. S. Zhang, G. Chang, I. Belopolski, Q. Zhang, T. A. Cochran, D. Multer, M. Litskevich, Z. J. Cheng, X. P. Yang, Z. Wang, R. Thomale, T. Neupert, S. D. Wilson & M. Z. Hasan. Unconventional chiral charge order in kagome superconductor KV3Sb5. *Nat Mater*, doi:10.1038/s41563-021-01034-y (2021).
- [32] Zuwei Liang, Xingyuan Hou, Fan Zhang, Wanru Ma, Ping Wu, Zongyuan Zhang, Fanghang Yu, J. J. Ying, Kun Jiang, Lei Shan, Zhenyu Wang & X. H. Chen. Three-Dimensional Charge Density Wave and Surface-Dependent Vortex-Core States in a Kagome Superconductor CsV3Sb5. *Physical Review X* **11**, doi:10.1103/PhysRevX.11.031026 (2021).
- [33] B. Q. Song et al. Competing superconductivity and charge-density wave in Kagome metal CsV3Sb5: evidence from their evolutions with sample thickness. *arXiv: 2105.09248* (2021).
- [34] Feng Du et al. Interplay between charge order and superconductivity in the kagome metal KV3Sb5. *arXiv: 2102.10959* (2021).
- [35] Yanpeng Song et al. Competition of superconductivity and charge density wave in selective oxidized CsV3Sb5 thin flakes. *arXiv: 2105.09898* (2021).
- [36] Han-Shu Xu et al. Multiband superconductivity with sign-preserving order parameter in kagome superconductor CsV3Sb5. *arXiv: 2104.08810*. (2021).
- [37] C. C. Zhao et al. Nodal superconductivity and superconducting domes in the topological Kagome metal CsV3Sb5. *arXiv: 2102.08356* (2021).
- [38] K. Y Chen, N. N Wang, Q. W Yin, Y. H Gu, K. Jiang, Z. J Tu, C. S Gong, Y. Uwatoko, J. P Sun, H. C Lei, J. P Hu & J. G. Cheng. Double Superconducting Dome and Triple Enhancement of Tc in the Kagome Superconductor CsV3Sb5 under High Pressure. *Physical Review Letters* **126**, doi:10.1103/PhysRevLett.126.247001 (2021).
- [39] F. H. Yu et al. Concurrence of anomalous Hall effect and charge density wave in a superconducting topological kagome metal. *arXiv: 2102.10987* (2021).
- [40] Zhiwei Wang et al. Anomalous transport and chiral charge order in kagome superconductor CsV3Sb5. *arXiv: 2105.04542* (2021).
- [41] Hui Chen et al. Roton pair density wave and unconventional strong-coupling superconductivity in a topological kagome metal. *arXiv: 2103.09188* (2021).
- [42] Shuo-Ying Yang, Yaojia Wang, Brenden R Ortiz, Defa Liu, Jacob Gayles, Elena Derunova, Rafael Gonzalez-Hernandez, Libor Šmejkal, Yulin Chen & Stuart SP Parkin. Giant, unconventional anomalous Hall effect in the metallic frustrated magnet candidate, KV3Sb5. *Science Advances* **6**, eabb6003 (2020).
- [43] E. M. Kenney, B. R. Ortiz, C. Wang, S. D. Wilson & M. J. Graf. Absence of local moments in the kagome metal KV3Sb5as determined by muon spin spectroscopy. *J Phys Condens Matter* **33**, doi:10.1088/1361-648X/abe8f9 (2021).

- [44] Xilin Feng, Kun Jiang, Ziqiang Wang & Jiangping Hu. Chiral flux phase in the Kagome superconductor AV₃Sb₅. *Science Bulletin*, doi:10.1016/j.scib.2021.04.043 (2021).
- [45] Hong Li et al. Rotation symmetry breaking in the normal state of a kagome superconductor KV₃Sb₅. *arXiv: 2104.08209*. (2021).
- [46] He Zhao et al. Cascade of correlated electron states in a kagome superconductor CsV₃Sb₅. *arXiv: 2103.03118*. (2021).
- [47] Nana Shumiya et al. Tunable chiral charge order in kagome superconductor RbV₃Sb₅. *arXiv: 2105.00550* (2021).
- [48] Hengxin Tan et al. Charge density waves and electronic properties of superconducting kagome metals. *arXiv: 2103.06325* (2021).
- [49] E. Liu, Y. Sun, N. Kumar, L. Muchler, A. Sun, L. Jiao, S. Y. Yang, D. Liu, A. Liang, Q. Xu, J. Kroder, V. Suss, H. Borrmann, C. Shekhar, Z. Wang, C. Xi, W. Wang, W. Schnelle, S. Wirth, Y. Chen, S. T. B. Goennenwein & C. Felser. Giant anomalous Hall effect in a ferromagnetic Kagome-lattice semimetal. *Nat Phys* **14**, 1125-1131, doi:10.1038/s41567-018-0234-5 (2018).
- [50] G. Kresse & J. Furthmuller. Efficient iterative schemes for ab initio total-energy calculations using a plane-wave basis set. *Physical Review B* **54**, 11169-11186, doi:10.1103/physrevb.54.11169 (1996).
- [51] P. E. Blöchl. Projector augmented-wave method. *Physical Review B* **50**, 17953-17979, doi:10.1103/PhysRevB.50.17953 (1994).
- [52] John P. Perdew, Kieron Burke & Matthias Ernzerhof. Generalized Gradient Approximation Made Simple. *Physical Review Letters* **77**, 3865-3868, doi:10.1103/PhysRevLett.77.3865 (1996).
- [53] S. Grimme, J. Antony, S. Ehrlich & H. Krieg. A consistent and accurate ab initio parametrization of density functional dispersion correction (DFT-D) for the 94 elements H-Pu. *J Chem Phys* **132**, 154104, doi:10.1063/1.3382344 (2010).
- [54] Ivo Souza, Nicola Marzari & David Vanderbilt. Maximally localized Wannier functions for entangled energy bands. *Physical Review B* **65**, 035109, doi:10.1103/PhysRevB.65.035109 (2001).
- [55] QuanSheng Wu, ShengNan Zhang, Hai-Feng Song, Matthias Troyer & Alexey A. Soluyanov. WannierTools: An open-source software package for novel topological materials. *Computer Physics Communications* **224**, 405-416, doi:10.1016/j.cpc.2017.09.033 (2018).